

Accepted by AJ, to appear in April 2001

AB Dor in '94: I. HST/GHRS Observations of the Quiescent Chromosphere of an Active Star

J.C. Brandt^{1,2}

*Laboratory for Atmospheric and Space Physics, Campus Box 392, University of Colorado,
Boulder, CO 80309-0392*

`jbrandt@lodestar.phys.unm.edu`

S.R. Heap¹

*Laboratory for Astronomy and Solar Physics, Code 681 NASA/Goddard Space Flight Center,
Greenbelt, MD 20771*

`hrsheap@stars.gsfc.nasa.gov`

F.M. Walter¹

State University of New York, Physics and Astronomy, Stony Brook, NY 11794-3800

`fwalter@astro.sunysb.edu`

E.A. Beaver¹

*Center for Astrophysics and Space Sciences C-0111, University of California, San Diego, La
Jolla, CA 92093-0111*

`ebeaver@ucsd.edu`

A. Boggess¹

2420 Balsam Dr. Boulder CO 80304

`boggess@lyrae.colorado.edu`

K.G. Carpenter¹

*Laboratory for Astronomy and Solar Physics, Code 681 NASA/Goddard Space Flight Center,
Greenbelt, MD 20771*

`carpenter@stars.gsfc.nasa.gov`

D.C. Ebbets¹

Ball Aerospace & Technologies Corp., P. O. Box 1062, AR1, Boulder, CO 80306

debbets@ball.com

J.B. Hutchings¹

Dominion Astrophysical Observatory, 5071 West Saanich Road, Victoria, BC, Canada V8X 4M6

john.hutchings@hia.nrc.ca

M. Jura¹

Department of Physics and Astronomy, University of California, Los Angeles, CA 90095-1562

jura@clotho.astro.ucla.edu

D.S. Leckrone¹

*Laboratory for Astronomy and Solar Physics, Code 681 NASA/Goddard Space Flight Center,
Greenbelt, MD 20771*

hrsleckrone@hrs.gsfc.nasa.gov

J.L. Linsky¹

*JILA, University of Colorado and National Institute of Standards and Technology, Boulder, CO
80309-0440*

jlinsky@jila.colorado.edu

S.P. Maran¹

Space Sciences Directorate, Code 600, NASA/Goddard Space Flight Center, Greenbelt MD 20771

hrsmaran@eclaire.gsfc.nasa.gov

B.D. Savage¹

*Department of Astronomy, University of Wisconsin, 475 North Charter Street, Madison, WI
53706*

bdsavage@facstaff.wisc.edu

A.M. Smith¹

*Laboratory for Astronomy and Solar Physics, Code 681 NASA/Goddard Space Flight Center,
Greenbelt, MD 20771*

hrssmith@hrs.gsfc.nasa.gov

L.M. Trafton¹

MacDonald Observatory and Astronomy Department, University of Texas, Austin, TX 78712

`lmt@astro.as.utexas.edu`

R.J. Weymann¹

*Observatories of the Carnegie Institution of Washington, 813 Santa Barbara Street, Pasadena CA
91101*

`rjw@ociw.edu`

D. Norman

State University of New York, Physics and Astronomy, Stony Brook, NY 11794-3800

`dnorman@sbast3.ess.sunysb.edu`

S. Redfield

JILA, University of Colorado, Boulder, CO 80309-0440

`sredfiel@casa.colorado.edu`

ABSTRACT

We analyze HST/GHRS spectra of AB Doradus, the prototypical ultra-rapidly rotating K dwarf. We observed chromospheric (Mg II) and transition region (C II, Si IV, C IV, and N V) lines periodically throughout the stellar rotation period, and provide a low dispersion stellar atlas of 78 emission lines. The quiescent line profiles of the chromospheric and transition region lines show narrow cores superposed on very broad wings. The broad wings of the Mg II *k* & *h* lines and of the transition region lines can be explained by emission from gas co-rotating with the star and extending out to near the Keplerian co-rotation radius (2.8 stellar radii). While this is not a unique solution, it is consistent with previous studies of H α emission that are naturally explained by large co-rotating prominences. We find no evidence for rotational modulation of the emission line fluxes. The density diagnostics suggest that the transition region is formed at constant pressure, with an electron density $2\text{--}3 \times 10^{12} \text{ cm}^{-3}$ at a temperature of $3 \times 10^4 \text{ K}$. The electron pressure is about 100 times larger than that for the quiet Sun. The emission measure distribution shows a minimum between $\log(T) = 5$ and 5.5. The Mg II

¹GHRS Investigation Definition Team

²Now at Department of Physics and Astronomy, Institute for Astrophysics, University of New Mexico, Albuquerque, NM 87131

line exhibits three interstellar absorption components along the 15 pc line of sight. We identify the lowest velocity component with the G cloud, but the other components are not identified with any interstellar clouds previously detected from other lines of sight.

Subject headings: stars: activity — stars: chromospheres — stars: individual(AB Dor)
— ISM: kinematics and dynamics

1. Introduction

We study magnetically-active solar-like stars because the characteristics of such stars may provide insights into the nature of solar-like magnetic activity. While we accept the solar paradigm, that stellar activity is a consequence of magnetic fields, it is not at all clear that any simple scaling of solar coronal structures can account for the level of activity seen in the most active stars. Indeed, the very assumption of solar-like structures may bias our interpretation of the observations. Walter & Byrne (1997), and Walter (1999) proposed a non-solar paradigm for active stars, based in part on observations of AB Doradus. In this picture, a quasi-dipolar global magnetic field may dominate the large-scale activity, while the hotter coronal gas is confined by solar-like magnetic structures to a small scale height. An active stellar atmosphere would then consist of a compact, solar-like chromosphere/transition region/corona and an extended, co-rotating envelope of large volume. Ayres et al. (1998) posit a similar picture for the magnetospheres of active Hertzsprung gap giants.

Ultraviolet spectra sample the chromosphere and transition region, at temperatures from about 10^4K through $2\times 10^5\text{K}$. While emission in the cooler lines may result in part from heating by acoustic fluxes, the transition region line emission is almost certainly from hot plasma trapped in magnetic loops. Time-resolved spectra obtained over a stellar rotation can yield important constraints on magnetic filling factors, global asymmetries, and atmospheric scale heights. Velocity-resolved line profiles can be inverted to yield spatial resolution on these stars, and images of their surfaces. Our goal, through detailed observations of highly active stars, is to test our understanding of stellar coronae and chromospheres, of the morphology of the magnetic field, and of its relation to the observed activity.

1.1. AB Doradus

AB Doradus (HD 36705; K0-2 IV–V), the brightest ($V=6.7$) of the ultra-rapid rotators ($P_{rot}=0.51479$ d; $v \sin i=91 \text{ km s}^{-1}$), is the quintessential active young single star. In addition to large flares (e.g., Robinson & Cameron 1986), large starspots (Anders et al 1992), and large coronal and chromospheric fluxes (Pakull 1981; Vilhu, Gustafsson, & Walter 1991), AB Dor also possesses co-rotating material at 2–5 stellar radii (Cameron & Robinson 1989), in the form of cool prominences or $\text{H}\alpha$ clouds (Cameron et al. 1990). Its brightness and activity levels make it an ideal target to study the extremum of stellar magnetic activity. Among the recent studies are those by Rucinski et al.

(1995b); Mewe et al. (1996); Kürster et al. (1997); Schmitt, Cutispoto, & Krautter (1998) Vilhu et al. (1998), and Ake et al. (2000).

The parallax (Guirado et al. 1997) places the star at 15 pc, slightly above the zero-age main sequence (Cameron & Foing 1997), with a probable age close to that of the Pleiades. AB Dor is a member of a multiple star system. The dMe4 star Rossiter 137B (AB Dor B) is a common proper motion companion at an angular distance of 10 arcsec (Innis et al. 1985; Innis, Thompson, & Coates 1986; Vilhu et al. 1989). Guirado et al. (1997) detected a low mass astrometric companion, AB Dor C, with an inferred separation of a few tenths of an arcsec. R 137B is outside the GHRS aperture; AB Dor C falls within the aperture, but is unlikely to make any significant contribution to the observed flux.

1.2. The November 1994 Campaign

We observed AB Dor with the Goddard High Resolution Spectrograph (GHRS; Brandt et al. 1994; Heap et al. 1995; Robinson et al. 1998) aboard the Hubble Space Telescope, as part of a multiwavelength campaign in November 1994 (Walter et al. 1995). Our goal was to obtain simultaneous spectroscopic and photometric observations at X-rays, UV, optical, and radio wavelengths over at least one stellar rotation period, in order to correlate the coronal, chromospheric, and optical behaviors, and to come up with a 3-dimensional picture of the atmosphere of a very active star.

The optical spectroscopy and photometry, and the Doppler images, have been reported by Cameron et al. (1999). AB Dor behaved normally (for AB Dor). There was a prominent photometric wave, indicating a highly asymmetric starspot distribution. We observed no large flares (i.e., flares with durations in excess of about an hour). Cameron et al. (1999) report a number of strong absorption events due to cool material (extended prominences) co-rotating at high altitude. The Doppler image (Cameron et al. 1999) shows a dark feature at high latitudes, with some low latitude spottedness. Vilhu et al. (1998) report a continuous GHRS observation of the C IV line which immediately preceded our observations.

We will report on the variability of the chromosphere and corona in a subsequent paper (Walter et al., in preparation). Here we present an analysis of the quiescent chromosphere of AB Dor as viewed over one stellar rotation period by the GHRS instrument on the HST.

2. The Observing Program and Data Reductions

We observed AB Dor (program 5181) with the HST/GHRS on 1994 November 14-15 while the target was in the continuous viewing zone. The observations began near the end of stellar rotation

cycle 10440³. Our strategy was to maximize spectral and temporal coverage by rapidly changing gratings to obtain a sequence of exposures during the 12.3 hour rotation period of AB Dor. For 12 hours we alternated between 256 second integrations of the Mg II lines, using the Echelle-B ($R \equiv \frac{\lambda}{\delta\lambda} \sim 100,000$), and 1228 second integrations of transition region lines using the G160M first order grating ($R \sim 20,000$). This strategy was driven by the one dimensional format of the GHRS detectors; at $R=20,000$ we observe only about 35\AA at a time.

The main observation was split into 6 sequences. Each sequence began with a peakup in the large aperture, to ensure that the target remained well-centered. Each sequence then consisted of 3 observations of the Mg II line alternating with observations of the Si IV $\lambda\lambda 1393,1402$ doublet, the C IV $\lambda\lambda 1548,1551$ doublet, and either the N V $\lambda\lambda 1238,1242$ doublet, the C II $\lambda\lambda 1334,1335$ doublet, or the density-sensitive Si III], C III] $\lambda\lambda 1892,1908$ intersystem lines. We concluded these six sequences with a final Si IV exposure sandwiched between two Mg II observations. All these observations utilized the D2 detector. At the end of these sequences, we changed to the D1 detector and observed the full short-wavelength spectrum ($1150\text{-}1750\text{\AA}$) at low dispersion in two G140L exposures. The details of the exposures are given in Table 1. Four observations were lost when the carousel failed to lock.

Each science observation was preceded by a spectral calibration lamp exposure which established the accurate wavelength scale. Occasional SPYBAL observations of the wavelength calibration lamps were also interspersed by the scheduling software. The target was observed through the large science aperture (LSA) using substep pattern 5. We calibrated the raw data using the GHRS team software procedure CALHRS (Blackwell et al. 1993). Each Mg II observation is a single spectrum, but each transition region spectrum consists of 4 independent spectra, providing about 5 minute temporal resolution. The analysis of the line profiles (excluding the Mg II ISM analysis in section 9) was carried out using the ICUR software package⁴. All the measurements (fluxes, centroids, Gaussian fits) use standard techniques.

Mewe et al. (1996) fit the EUVE and ASCA spectra, and found a best fit absorption column of $2.4 \pm 0.5 \times 10^{-18} \text{ cm}^{-2}$. Since the reddening correction is less than 1%, we do not apply any reddening corrections.

3. The Low Dispersion Spectral Atlas

The summed low dispersion spectrum is shown in Figure 1. Two spectra centered at 1305\AA and 1571\AA cover almost all the useful wavelength range of the G140L grating ($1162\text{-}1714\text{\AA}$) with 20\AA of overlap in the middle. The resolution of this spectrum, $R \sim 2000$, is adequate to resolve most astrophysically-important blends, including (marginally) the C II $\lambda 1334,1335$ doublet. We obtained

³using the ephemeris $\text{HJD} = 2444296.575 + 0.51479\text{E}$

⁴<http://sbast3.ess.sunysb.edu/fwalter/ICUR/icur.html>

this spectrum primarily for the purpose of constructing the line atlas (Table 2), and to determine the emission measure distribution (Section 8) of the chromosphere of this very active star.

The spectrum shows a wealth of detail, including weak lines of neutral and low-ionization species, the strong transition region lines, and the Fe XXI coronal line. We have identified the emission lines using the solar line lists of Burton & Ridgeley (1970) and Feldman et al. (1997). Other possible identifications are found in the CHIANTI (Dere et al. 1997) database. The brightest stellar emission line is He II $\lambda 1640$ (the H I Lyman α emission is geocoronal). Identifications for some of the weaker lines and blends are uncertain, and will require higher dispersion spectra for definitive identification.

There are 63 lines in Table 2 with secure identifications. The mean difference between the observed and tabulated (rest) wavelengths is $0.15 \pm 0.02 \text{ \AA}$, corresponding to a radial velocity of $33 \pm 5 \text{ km s}^{-1}$, in good agreement with the previously-measured photospheric value of 30 km s^{-1} . Much of the scatter lies, as expected, in the weaker lines. The mean radial velocity of the 34 strongest lines (fluxes $> 1.0 \times 10^{-14} \text{ erg cm}^{-2} \text{ s}^{-1}$) is also $33 \pm 5 \text{ km s}^{-1}$. This agreement with the photospheric radial velocity verifies both that the wavelength scale is accurate and that the line identifications are most likely correct.

4. The $\lambda 1900 \text{ \AA}$ Region

Figure 2 shows the mean spectrum in the $\lambda 1900 \text{ \AA}$ region. The two G160M observations were obtained at rotational phases 0.336 and 0.800, and sample opposite hemispheres of the star. The $\lambda 1900 \text{ \AA}$ continuum is 46% brighter at phase 0.8. The contemporaneous U and V band photometry (Rucinski, Garrison, & Duffee 1995a; Cameron et al. 1999) shows that the star was faintest at about rotation phase 0.5, and that in the U band AB Dor is about 15% brighter at phase 0.8 than at phase 0.34. There is no significant change in the emission line fluxes between the two observations.

In addition to the expected Si III] $\lambda 1892$ and C III] $\lambda 1908$ intersystem lines, we see four narrow lines of S I and a line of Si I (Table 3, Figure 2). The possible feature at 1907.3 \AA (1907.1 \AA rest wavelength) is unidentified. The C III] $\lambda 1908$ line is much broader than the other lines (see Section 7.4). The line widths listed in Table 3 are measured by fitting Gaussians to the lines. A line broadened by the stellar rotation would have a FWHM of approximately 0.8 \AA in this spectral region (assuming a 40% overestimate of $v \sin i$ from the Gaussian fit: see discussion in Section 5).

5. Transition Region Quiescent Line Profiles

We monitored the transition region doublets of C II, Si IV, C IV, and N V. The Si IV and C IV lines were each observed six times, and exhibited variability. Each observation consisted of four

~ 5 minute integrations, which permits us to examine the data for line profile variations or flaring on timescales of 5 to 20 minutes. We examined the individual integrations for evidence of flaring (rapid flux variations over the 4 integrations, varying line profiles, or fluxes significantly in excess of the median). We generated quiescent line profiles by summing those spectra which had fluxes near the median, symmetric line profiles, and no evidence for flaring. In Figure 3 we compare the 4 quiescent line profiles. Here we discuss only the quiescent line profiles; we will discuss the flaring spectra elsewhere.

We initially fit the emission lines as Gaussians or sums of Gaussians because this approach is commonly used and the resulting fits are generally quite acceptable. Vilhu et al. (1998) found that the C IV emission lines could be fit as a sum of narrow and broad Gaussian components (as found in general by Wood, Linsky, & Ayres 1997). The narrow components are significantly broader than the expected rotational broadening, and Vilhu et al. interpreted this nonthermal broadening in terms of solar-like nonthermal broadening mechanisms (e.g., Dere & Mason 1993), perhaps related to microflares. Unlike the case of the Sun, we do not know much about the spatial distribution of the emitting gas. It probably is not confined to a thin region, given the evidence for extended prominences, in which case the atmosphere is extended and interpretation of line profiles is not straightforward.

We simulated line profiles from photospheres (with limb darkening parameters $-1.0 < \epsilon < 1.0$) and from optically-thin extended co-rotating atmospheres, convolved them with the expected thermal broadening and with a Gaussian instrumental response, and fit the lines as Gaussians. In the case of $\epsilon=0.6$ we recover the well-known rotational profile (e.g., Gray 1992); $\epsilon=0.0$ is a uniform disk, and $\epsilon < 0$ yields limb-brightened profiles. Transition region lines are more likely optically thin emission from an extended atmosphere. We also examined cases where the emission is confined to low latitudes. Limb-brightened atmospheres tend to produce flat-peaked line profiles (for modest extents of $\lesssim 10\%$ of the stellar radius), whereas limb-brightened atmospheres with emission confined to low latitudes produce emission cusps for sufficiently large $v \sin i$.

Although the intrinsic line profiles are not Gaussian, significant noise and low resolving power allow Gaussian fits to be acceptable in many cases. The widths of the Gaussian fits always exceed $v \sin i$. We find that for photospheric line profiles, the Gaussian fits overestimate $v \sin i$ by up to 40%, depending on the value of ϵ and the intrinsic $v \sin i$. Gaussian fits to limb-brightened profiles (containing a few thousand counts) overestimate the $v \sin i$ by 40-80%. Dere & Mason (1993) showed that optical thickness will also tend to broaden the line profiles; in slightly thick but effectively thin lines, photons from the line core will be scattered into the wings. We caution the reader that the interpretation of emission line profiles is highly model dependent. Consequently, we do not interpret the width of the narrow emission component of the transition region lines.

In Figure 4 we show the subordinate ($3p \ ^2P_{\frac{1}{2}} - 3d \ ^2D_{\frac{3}{2}}$) Mg II line at $\lambda 2791.6\text{\AA}$, which is almost certainly optically thin. The profile is flat-topped, and at resolution $R \sim 10^5$ the shape of the line profile is clearly not Gaussian. The rotation profile for a limb-darkened photosphere is much

more sharply peaked. Figure 4 demonstrates that this line can be produced by a limb-brightened, optically thin atmosphere with a height of a few percent of the stellar radius. This fit is not unique: within the uncertainties one could also fairly well reproduce the profile with, for example, a rotating photospheric profile ($\epsilon=0.6$) with no emission above about 30° latitude, or a uniform disk profile ($\epsilon=0.0$) with emission confined below about 60° latitude.

The strong resonance lines of the transition region clearly cannot be fit with a single component. Instead we fit the lines as sums of narrow and broad Gaussians. We find that we get better fits with three components: a broad component and two similar narrow Gaussians displaced from line center by about $\pm 0.5 v \sin i$. This model gives better fits because the peaks of the Si IV and C IV are flatter than a Gaussian profile. Physically, this is because in an extended limb brightened atmosphere the centroid of the emission is displaced to higher velocities where the path length through the atmosphere is longer. We also have had success in fitting the line wings with emission from an optically thin, extended, rigidly-rotating atmosphere (see Section 5.5).

5.1. C IV

We identified 17 of the 24 C IV integrations as likely to represent the non-flaring, quiescent transition region. The C IV flux (the sum of the fluxes in the $\lambda\lambda 1548, 1551$ lines) during quiescence is less than 1.5×10^{-12} erg cm $^{-2}$ s $^{-1}$. Vilhu et al. (1998) noted that the non-flaring flux level just prior to our observation ranged between 1.0 and 1.5×10^{-12} erg cm $^{-2}$ s $^{-1}$, and the average C IV flux during our entire observation is 1.2×10^{-12} erg cm $^{-2}$ s $^{-1}$. The $\lambda\lambda 1549/1551$ line ratio of 1.78 ± 0.03 is close to but less than the optically thin limit.

The summed quiescent line profile (Figure 5) should represent the phase-averaged transition region. Although we can fit the line with a sum of two Gaussians with fit parameters similar to those of Vilhu et al. (1998), we find that the data are better fit with three components. We plot neither the 2- or 3-component Gaussian fits to this or any line in Figures 5 to 7. Rather, the fits to the high velocity wings shown in Figure 5 are for optically thin, constant density atmospheres extending out 2.5 stellar radii. Forty percent of the total flux is in the extended component.

5.2. Si IV

The mean Si IV $\lambda 1393$ line flux is 2.2×10^{-13} erg cm $^{-2}$ s $^{-1}$. From a visual examination of the line profiles and the line fluxes, we identified 20 quiescent spectra, and summed these (Figure 6). The $\lambda\lambda 1393/1402$ line ratio of 1.78 ± 0.02 is identical to that in the C IV lines. Although close to the optically thin limit, both line ratios are significantly less than 2. This probably indicates that at least some of the emission is from optically thick regions.

Because the lines are well separated and because the blue wing of the $\lambda 1402$ line is blended

with O IV] $\lambda 1401.34$, we fit only the $\lambda 1393$ line. As with the C IV lines, the Si IV line profile is better fit with a broad component centered on the rest velocity of the star plus two narrow emission components than it is with a two-Gaussian model. If we fit the high velocity wings as emission from extended gas (see Figure 6), we find that the emission extends out to 3 stellar radii, which is comparable to what we found for C IV. About 25% of the Si IV emission is in the extended component.

5.3. N V

We obtained a single G160M observation of the N V doublet at phase 0.5. The line fluxes are 95% of those seen in the low dispersion spectrum. The line ratio of 2.10 ± 0.04 is consistent with the line's being optically thin. There is no evidence for the broad component seen in the Si IV and C IV lines, perhaps because of the low S/N in this integration. However, there is a small flux excess on the red side of the $\lambda 1242\text{\AA}$ line. This is not seen on the blue side of the line, nor is it obvious in the $\lambda 1238\text{\AA}$ line. The cause could be a downflow, or perhaps a small flare on the receding limb of the star.

5.4. C II

We obtained a single G160M observation of the C II doublet at phase 0.65. The emission lines are severely blended, and we were unable to fit the various components uniquely. High velocity wings are evident. There is a strong interstellar absorption feature in the $\lambda 1334.5\text{\AA}$ line, with a radial velocity of $9 \pm 3 \text{ km s}^{-1}$. Given the resolution of the GHRS in this mode, it is not possible to identify the absorption with any particular component of the interstellar medium (see Section 9). Corresponding (though much weaker) absorption is seen near the top of the $\lambda 1335.7\text{\AA}$ line.

This spectrum also shows the S I $\lambda 1323.52$, C I $\lambda 1329.1$, and Cl I $\lambda 1351.66$ lines with fluxes similar to those in Table 2.

5.5. Discussion of the Transition Region Lines

The transition region lines of active stars are generally modeled as the sum of broad and narrow Gaussians. The width of the narrow component is generally significantly broader than the stellar $v \sin i$, and this is interpreted as the convolution of the stellar rotational profile with some other broadening mechanism. Wood, Linsky, & Ayres (1997) showed that among dwarf stars, the excess broadening appears to decrease with increasing surface gravity ($\xi_{NC} \propto g^{-0.68}$). The broad component is often interpreted as evidence for high velocity gas associated with microflaring.

We have difficulty interpreting the line profiles of AB Dor in this manner. After deconvolving

the 90 km s^{-1} rotational velocity from the narrow central emission component we find that the velocity of the excess broadening mechanism is about 120 km s^{-1} , which places AB Dor well above the trend found by Wood, Linsky, & Ayres (1997) for less active stars. And while microflaring may indeed exist and contribute to the width of the broad component, the evidence for spatially extended gas leads us to propose a fundamentally different mechanism for the broad line component.

We propose that the high velocity wings are due to spatially-extended gas co-rotating with the star, and not to some unknown broadening mechanism. The existence of extended prominences seen in the light of $\text{H}\alpha$ is well established; it is likely that this same gas accounts for the extended wings of the $\text{Mg II } k\&h$ lines. The wings of the transition region lines have very similar shapes, suggesting that these lines also have a similar origin. Corroborating evidence for extended hot gas hot gas exists: Walter et al. (1995; 2001 in preparation) show that C IV undergoes absorption events associated with $\text{H}\alpha$ prominences.

We model the extended gas as a simple optically thin volume co-rotating with the star, and assume that the density is uniform between some inner and outer radii. The emission from each point is broadened by a thermal velocity appropriate to the ion in question. The computed profiles do not depend sensitively on the value of the assumed inner radius, since the emission from gas close to the star is hidden by the central emission component, but the outer radius does determine the width of the broad line component. We vary only the outer radius to match the observations. We can also vary the extent of the gas in latitude, but we are not very sensitive to this because gas at high latitudes has smaller velocities, and is buried under the central emission.

The inferred radial extent of the extended gas is close to the Keplerian co-rotation radius of 2.8 stellar radii. We favor a model in which the gas is trapped by large-scale quasi-dipolar magnetic fields (Walter 1999). Such gas will be most stable near the co-rotation radius (e.g., the “slingshot prominences” of Cameron & Robinson 1989).

Assuming that the gas is optically thin and in rigid rotation, we can use the high velocity wings to estimate the mean electron density in the extended gas. The mean electron density n_e is given by $0.8 \sqrt{\frac{L}{PV}}$, where L is the velocity-resolved luminosity of the line, P is the power in the line, V is the velocity-resolved volume element, and the 0.8 factor accounts for the fact that hydrogen is largely ionized. The mean density is about $5 \times 10^7 \text{ cm}^{-3}$ at the temperature of the transition region lines for a filling factor of 1; the presence of discrete prominences suggests that the filling factor of this extended region is very low, and the density in the prominences must be commensurately larger.

We see no evidence for any rotational modulation of the fluxes in the Mg II , C IV , or Si IV lines. The photosphere is faintest at rotation phase 0.5 (Cameron et al. 1999). Following solar analogy, the dark regions (starspots) are likely regions of larger photospheric magnetic flux and the bright chromosphere and transition region should be located above the starspots. If the chromosphere and transition region are spatially extended, as is likely the case here, then any modulation would be diluted. Our data let us place a limit of 5% on the amplitude of the rotational modulation in

the chromospheric and transition region lines.

6. The Mg II lines

6.1. The Chromospheric Mg II Emission

We observed the chromospheric Mg II *k* & *h* lines 19 times, approximately every 35-50 minutes, with a resolving power of about 10^5 . The mean profile of the two lines is presented in Figure 7. The *k* & *h* resonance lines are well-exposed, and the Mg II subordinate lines are detected as well. Both the *k* & *h* lines exhibit extended blue wings, to velocities of about -320 km s^{-1} with respect to the star. The red wings cannot be measured because the *k* line is blended with the subordinate lines, and the red wing of the *h* line falls off the edge of the detector. The brightness ratio near line center is 1.23, confirming that the line cores are optically thick, and the *k* line has brighter line wings as expected for the higher opacity line. Over 10% of the flux in the line core is lost to the narrow interstellar absorption lines (cf. Section 9).

Since Mg II is formed in the chromosphere, at about the same temperature as $\text{H}\alpha$, one might expect to see absorption events in Mg II similar to those seen in $\text{H}\alpha$ (Cameron et al. 1990, 1999), and indeed we do see such absorption events. These will be discussed elsewhere (Walter et al. 2001, in preparation). The same prominences seen in absorption against the stellar disk should be seen in emission off the limb, and may account for the broad wings of the *k* & *h* lines. The maximum velocity is consistent with emission from gas in co-rotation at heights of up to 3.5 stellar radii. In Figure 7 we overplot the expected emission line profile, scaled to the data, for a co-rotating atmosphere extending to a height of 3 stellar radii. This is neither a fit to the data, nor it is a unique description of the data, but it demonstrates that the extended wings could arise from an extended atmosphere without assuming non-thermal broadening mechanisms. This extended emission accounts for 20% of the total Mg II *k* & *h* emission, after correcting for the interstellar absorption. The mean density in the extended atmosphere at chromospheric temperatures is about $3 \times 10^8 \text{ cm}^{-3}$ (for a filling factor of 1). This is about a factor of 6 higher than the density inferred from the transition region lines, and within the uncertainties is consistent with a constant pressure atmosphere.

7. The Density Diagnostics

The mean density at a given temperature provides clues to the gross morphology of the stellar atmosphere, since the emission measure ($\int n_e n_H dV$) depends on both the density and the volume. Even at very low spatial resolution, the observed density can help us discriminate between compact high density emitting regions and large extended structures. There are a number of density diagnostics in this region of the spectrum (e.g., Doschek et al. 1978). We use the line strengths

in Tables 2, 3, and 4 to compute the density sensitive line ratios, and use the CHIANTI software package to convert the line ratios to densities.

7.1. Densities involving the Si III lines

We used 3 Si III lines and the sum of the $\lambda\lambda 1294\text{--}1301$ lines to form 4 line ratios. These consistently yield densities between 2 and $3 \times 10^{12} \text{ cm}^{-3}$ at a temperature of about $3 \times 10^4 \text{ K}$ (Table 5).

7.2. Densities involving the C III lines

Cook & Nicolas (1979) discuss using the C III lines to determine densities. We use the $\lambda 1175$, 1247, and 1908Å lines in this analysis. The densities are not mutually consistent (Table 5). Cook & Nicolas (1979) note that in the Sun the density ratios involving the $\lambda 1175$ line are consistently off, perhaps because the $\lambda 1175$ line intensity is reduced by optical depth effects. An increase of about a factor of two in the $\lambda 1175$ line flux would bring the $\frac{\lambda 1175}{\lambda 1908}$ density into agreement with the $\frac{\lambda 1247}{\lambda 1908}$ density, at about 10^{11} cm^{-3} . The $\frac{\lambda 1175}{\lambda 1247}$ density would then become about $5 \times 10^{11} \text{ cm}^{-3}$.

Using the $\frac{1175}{977}$ line ratio, Schmitt, Cutispoto, & Krautter (1998) and Ake et al. (2000) both infer densities at the high density limit, $> 10^{11} \text{ cm}^{-3}$, which is consistent with our estimates.

The densities inferred from the C III lines (formed at $6 \times 10^4 \text{ K}$) are smaller than those inferred from Si III (formed at about $3 \times 10^4 \text{ K}$): in a constant pressure atmosphere they should have about half the density indicated by the Si III lines. This would be consistent with a model in which the bulk of the transition region emission arises in constant pressure loops.

Cook & Nicolas (1979) also estimate densities from ratios of Si III] $\lambda 1892$ and Si IV $\lambda 1402$ to C III] $\lambda 1908$. These densities are valid so long as the relative abundances are solar. The $\frac{\lambda 1892}{\lambda 1908}$ ratio has traditionally been used as a density diagnostic in IUE spectra (Doschek et al. 1978). We find this ratio to be about 1.3, which suggests a density near $3 \times 10^{10} \text{ cm}^{-3}$, but the $\frac{\lambda 1402}{\lambda 1908}$ ratio implies a density nearer $3 \times 10^{11} \text{ cm}^{-3}$, using Cook & Nicolas’ model atmosphere ratios. Note that the Si III] $\lambda 1892$ and C III] $\lambda 1908$ line profiles are very different (Figure 2), with the C III] line nearly twice as broad, suggesting that they might not be formed co-spatially.

7.3. Densities from the $\lambda 1400\text{Å}$ region

The $\lambda 1400\text{Å}$ region (Figure 8) includes a number of density-sensitive O IV] (Cook et al. 1995) and S IV] (Dufton et al. 1982) intercombination lines. These lines are much weaker than the nearby Si IV resonance lines. The $\lambda 1399.8$ and $\lambda 1401.2$ O IV] lines are clearly visible in the low dispersion spectrum, blended with the blue wing of Si IV $\lambda 1402.8$. We estimated their fluxes first by fitting

all 3 lines, forcing the wavelengths and line widths of the O IV] lines to their expected values. Since the two Si IV lines should have identical profiles, we then shifted, scaled, and subtracted the Si IV $\lambda 1393.8$ from the Si IV $\lambda 1402.8$ line profile, and fit the residuals. The $\lambda 1407.4$ O IV] line is also visible in the low dispersion spectrum. These fluxes can be found in Table 2.

We also searched for these lines in the summed G160M spectrum (total exposure time = 7368s). This spectrum is a global average over all rotational phases. Although flaring affects the strong Si IV resonance line profiles and fluxes, we find no evidence of enhanced emission in the weaker lines during flares. As in the low dispersion image, there is clear evidence for extra emission on the blue wing of the Si IV $\lambda 1402.8$ line. Using the same multi-line fitting procedure, we measure the line fluxes given in Table 4. We note that high dispersion does not improve the flux measurements significantly, because the lines are over-resolved due to rotational line broadening, and the rotational line broadening causes line blending.

We measure the $\frac{\lambda 1399.8}{\lambda 1407.4}$ line ratio to be 2.1 ± 0.5 , which is marginally consistent with the expected value of 0.993. Due to the poor accuracy of the flux determinations, the density diagnostics are inconclusive. Similarly, the S IV line ratios are inconclusive. The S IV $\lambda 1423.9$ line is blended at low resolution with a stronger S I line. Although there is a weak line near $\lambda 1416.9$ in the low dispersion spectrum, no line of similar strength is seen in the higher resolution spectrum.

7.4. The Densities of AB Dor

The densities listed in Table 5 range from about 10^9 cm^{-3} to $3 \times 10^{12} \text{ cm}^{-3}$. The densities derived from the four line ratios using the Si III lines are self-consistent but larger than the other diagnostics, while those involving C III] $\lambda 1908$ are systematically low. As discussed above, an arbitrary doubling of the C III] $\lambda 1175$ line flux (justified because it appears to work for the Sun) brings the $\frac{\lambda 1175}{\lambda 1247}$ density into better agreement with the Si III densities (Table 5), while leaving all the densities based on C III] $\lambda 1908$ consistently lower by about an order of magnitude.

The systematically lower densities indicated by the ratios involving the C III] $\lambda 1908$ line can be reconciled if the C III] $\lambda 1908$ line is preferentially formed in the extended, low density region near the co-rotation radius. This would explain both the significant broadening of the C III] $\lambda 1908$ line, and the enhanced line strength. The FWHM of the C III] $\lambda 1908$ line (Table 3) corresponds to about $3 v \sin i$, and so is consistent with formation in a region close to the co-rotation radius. We believe that the most reliable density estimate is $n_e = 2-3 \times 10^{12} \text{ cm}^{-3}$ from the Si III line ratios because of the consistency among the four ratios. The electron pressure at 30,000K would then be $P_{e=n_e T} = 6-9 \times 10^{16} \text{ cm}^{-3} \text{ K}$, about 100 times the value for the quiet Sun.

8. The Emission Measure Distribution

We present an emission measure distribution based on the observed line fluxes in Figure 9. We use the line emissivities tabulated by Landini & Monsignori Fossi (1990), interpolated with a cubic spline. Landini & Monsignori Fossi computed the line emissivities in the low density limit. Since much of the flux seems to arise in a high density atmosphere, we used the CHIANTI database to determine the relative emissivities at low and high densities, and used this to determine proper emissivities for the few density-sensitive lines. The emission measure curves in Figure 9 assume $n_e=10^{12} \text{ cm}^{-3}$.

In this diagram, we have overplotted the $T^{\frac{3}{2}}$ extrapolation of the coronal emission measure, for $\int n_e n_H dV = 3 \times 10^{52} \text{ cm}^{-3}$ at $\log T = 6.6$ (Rucinski et al. 1995b; Mewe et al. 1996). We have also added the far UV line fluxes from ORFEUS II (Schmitt, Cutispoto, & Krautter 1998), after multiplying the ORFEUS II fluxes by 1.1 to bring their C III $\lambda 1175$ and Si III $\lambda 1206$ fluxes into agreement with our measurements. The extrapolation of the emission measure of the cooler coronal component is in good agreement with the fluxes of the C III, C IV, N V, and O VI lines, especially considering the non-simultaneity of the UV, FUV, and X-ray observations.

A number of lines seem to have emission measures above the minimum. The cool C, Si, and S lines may either form at temperatures below $\log(T)=4.2$, or they may derive much of their flux from a large extended volume. Three other lines are clearly out of place.

- C III] $\lambda 1908$ implies an emission measure 1.5 orders of magnitude larger than that of the other C III lines, which are consistent with the trends from other species. No more than a few percent of the C III] $\lambda 1908$ flux can be generated at these high densities due to strong collisional de-excitation; the remainder of the flux may arise in an extended lower density region.
- He II $\lambda 1640$ is far too strong to be formed in collisional equilibrium at a temperature near 10^5 K (Jordan 1975), given the emission measure at this temperature. This line is more likely formed during recombination following ionization of He I by coronal X-rays shining down on the lower chromosphere at $T \sim 10^4 \text{ K}$ (Zirin 1975; Laming & Feldman 1993; Wahlstrøm & Carlsson 1994).
- The O V $\lambda 1371$ line suggests a very small emission measure. The line emissivity in Landini & Monsignori Fossi (1990) suggests that the line should be an order of magnitude *brighter* than is observed. The O V emission measure is inconsistent with the O IV and O VI line emission measures.

Note that the strong transition region resonance lines of Si IV, C IV, and N V suggest emission measures somewhat above the minimum values indicated by other ions. We suggest that the excess flux, that above the minimum in the emission measure diagram, may arise in the spatially-extended gas near the co-rotation radius.

9. The Interstellar Absorption Features

There is considerable evidence that the Sun lies inside a small cloud, called the Local Interstellar Cloud (LIC), of warm partially ionized gas moving with a single-valued bulk flow velocity of -26 km s^{-1} from Galactic coordinates $l^{\text{II}} = 186^\circ$ and $b^{\text{II}} = -16^\circ$, roughly the direction of the Sco-Cen association (Crutcher 1982; Lallement et al. 1995; Redfield & Linsky 2000). In spectra of nearby stars, narrow interstellar absorption features with velocities equal to the projected velocity of the LIC vector are identified as absorption from this cloud along the line of sight to the star. Other nearby clouds that have been identified include the G Cloud, so named because it lies in the direction of the Galactic center (Lallement & Bertin 1992), and clouds in the direction of the North Galactic Pole and South Galactic Pole (Redfield & Linsky 2000). Observations of $\alpha \text{ Cen}$ and 36 Oph indicate that the interface between the LIC and the G Cloud is located $< 0.19 \text{ pc}$ from the Sun roughly in the direction of the Galactic Center (Linsky & Wood 1996; Wood, Linsky, & Zank 2000). A three-dimensional model of the LIC was developed by Redfield & Linsky (2000) based on 32 lines of sight using HST, EUVE, and ground based Ca II spectra. In their model, the LIC extends about 5 pc in the anti-Galactic Center direction, and a fraction of a parsec in the Galactic Center direction, so that the Sun is located just inside the very edge of the LIC. For the line of sight toward AB Dor, the model predicts the presence of very little LIC material.

The Mg II lines of AB Dor contain two broad interstellar absorption features. We fit the ISM features in the mean Mg II h and Mg II k lines simultaneously to maximally constrain the heliocentric velocity v (km s^{-1}), the Doppler parameter b (km s^{-1}), and the Mg II column density $\log N_{\text{MgII}}$ ($\log \text{cm}^{-2}$). The best fit is illustrated in Figure 10. To estimate the “continuum” against which the absorption features are measured, we use observed fluxes on either side of the absorption features and fluxes derived from mirroring the red-side of the line together to fit a fifth-degree polynomial. This “continuum” is shown in Figure 10 as the thin solid line. For a given set of interstellar parameters (v , b , N_{MgII}), the profiles for the interstellar absorption features were computed and then convolved with the echelle-B LSA instrumental profile (Gilliland & Hulbert 1993). In Figure 10 the absorption profiles of the individual ISM components are shown as dotted lines, and the convolution of these components with the instrumental profile is shown as the thick solid line. A scattered light correction was made by simply subtracting a small flux level across the whole spectrum. Numerous fits were made with different estimates of the scattered light correction factors in order to estimate the systematic errors. For the most part, the uncertainties are dominated by the random error. The derived parameters for these interstellar absorption components are listed in Table 6.

The two broad interstellar absorption features in the Mg II lines can be resolved into three different components – one with a heliocentric velocity of 5.17 km s^{-1} and the other two with velocities of 14.5 and 19.6 km s^{-1} . A two component model inaccurately fits the high velocity feature in the Mg II k line, so a third component was added to adequately fit the flattened appearance of the high velocity absorption feature between 14 and 19 km s^{-1} . Since the quality-of-fit does not improve significantly with the addition of a fourth component, the data do not require more

than three components. With a Galactic longitude of $l^{\text{II}} = 275^\circ$ and a latitude of $b^{\text{II}} = -33^\circ$, the projected LIC velocity toward AB Dor should be 4.25 km s^{-1} and the corresponding G Cloud velocity should be 5.29 km s^{-1} . Because the projected velocities of the LIC and G Cloud are so similar in value, it is difficult to interpret the observed 5.17 km s^{-1} component as being associated with only one or the other cloud. The fit itself seems to favor the G Cloud projected velocity vector, and based on the LIC model and observations of other nearby stars (α Cen and 36 Oph) we expect very little LIC material along this line of sight. The LIC model predicts a hydrogen column density of $\log N_{\text{HI}} = 16.88$ (Redfield & Linsky 2000). Using a typical magnesium depletion for the LIC of $D(\text{Mg}) \sim -1.1 \pm 0.2$ from Piskunov et al. (1997), the predicted Mg II column density contribution of the LIC in the direction of AB Dor is only $\log N_{\text{MgII}} \sim 11.4 \pm 0.2$, where $D(\text{Mg}) = \log(N_{\text{MgII}}/N_{\text{HI}}) - \log(\text{Mg}/\text{H})_{\odot}$. Therefore, the LIC should be a small contributor to the observed 5.17 km s^{-1} interstellar absorption component. However, if this absorption component is associated with the G Cloud, the large Doppler parameter, $b = 3.8 \text{ km s}^{-1}$, implies a large turbulent velocity. If we assume a temperature typical for the G Cloud, $T = 5650 \text{ K}$, based on observations of α Cen and 36 Oph (Linsky & Wood 1996; Wood, Linsky, & Zank 2000), the turbulent velocity is then $\xi = 3.3 \text{ km s}^{-1}$, where we have used the equation $b^2 = (0.0165T/A + \xi^2)$ with $A = 24.3$ for magnesium. Other turbulent velocities measured for the G Cloud by Linsky & Wood (1996) and Wood, Linsky, & Zank (2000) have significantly lower magnitudes. This high turbulent velocity could be caused by a shearing of the gas, possibly near the interface of the cloud. However, it is more likely that because the LIC and G Cloud projected velocities are so close, we are unable to differentiate between them in the spectrum. Both clouds may be contributing to the broad absorption feature, leading to the appearance of a large Doppler parameter and turbulent velocity if the absorption is ascribed to only one cloud. The observed 14.5 and 19.6 km s^{-1} components have not yet been identified with any previously detected cloud.

10. Summary

We have presented the overall quiescent characteristics of AB Doradus as it appeared during our 1994 November HST/GHRS observations. The transition region and Mg II line profiles provide evidence for significant amounts of material co-rotating with the star out to at least 3 stellar radii with temperatures extending from the lower chromosphere to at least 10^5 K . This picture supports a model with extended gas confined near the Keplerian co-rotation radius (2.8 stellar radii) by large-scale magnetic fields. We surmise that most of the detected emission, the $\sim 60\text{--}80\%$ emitted in the narrow line component, arises in high density, small scale height regions close to the photosphere. The extended material may well be at a lower density, as indicated by the low density derived from the $\frac{\text{Si III] } \lambda 1892}{\text{C III] } \lambda 1908}$ line ratio, since both lines are depleted at high density (with the C III] line depleted faster). Formation of the C III] $\lambda 1908$ line in the low density extended gas would explain both the broad line profile and the large flux.

These quiescent spectra alone contain a wealth of information, and show that high signal-to-

noise, high dispersion spectra of magnetically active stellar chromospheres and coronae provide important insights into the spatial morphology of the stellar magnetospheres. In particular, we can determine the emission measure distribution, the atmospheric densities, the spatial extent of the atmosphere, and the properties of the interstellar medium along the line of sight. High signal-to-noise, high dispersion UV spectra of active stars provide our best indication of the conditions from which our present day solar atmosphere evolved.

This paper is based on observations made with the NASA/ESA *Hubble Space Telescope*, obtained at the Space Telescope Science Institute, which is operated by the Association of Universities for Research in Astronomy, Inc., under NASA contract NAS 5-26555. This research was supported primarily by NASA grant NAG51862 to SUNY Stony Brook. We also acknowledge support to the University of Colorado through grant S-56460-D. We thank the many people who contributed to the success of the HST and GHRS programs.

REFERENCES

- Ake, T.B., Dupree, A.K., Young, P.R., Linsky, J.L., Malina, R.F., Griffiths, N.W., Siegmund, O.H.W., & Woodgate, B.E. 2000, *ApJ*, 538, L87
- Anders, G.J., Coates, D.W., & Thompson, K. 1992 *Proc. Astron. Soc. Australia*, 10, 33
- Ayres, T.R., Simon, T., Stern, R.A., Drake, S.A., & Brown, A. 1998, *ApJ*, 496, 428
- Blackwell, J., Shore, S.N., Robinson, R.D., Feggans, K., Lindler, D.J., Malumuth, E., Sandoval, J., & Ake, T.B. 1993, *A User's Guide to the GHRS Software* (version 2.1; Greenbelt MD: GSFC)
- Brandt, J.C., et al. 1994, *PASP*, 106, 890
- Burton, W.M. & Ridgeley, A. 1970, *Sol. Phys.*, 14, 3
- Cameron, A., Duncan, D.K., Ehrenfreund, P., Foing, B.H., Kuntz, K.D., Penston, M.V., Robinson, R.D., & Soderblom, D.R. 1990, *MNRAS*, 247, 415
- Cameron, A.C. & Foing, B. 1997, *Observatory*, 117, 218
- Cameron, A. & Robinson R.D. 1989, *MNRAS*, 238, 657
- Cameron, A., et al., 1999, *MNRAS*, 308, 493
- Cook, J.W., Keenan, F.P., Dufton, P.L., Kingston, A.E., Pradhan, A.K., Zhang, H.L., Doyle, J.G., & Hayes, M.A. 1995, *ApJ*, 444, 936
- Cook, J.W. & Nicolas, K.R. 1979, *ApJ*, 229, 1163
- Crutcher, R.M. 1982, *ApJ*, 254, 82
- Dere, K.P., Landi, E., Mason, H.E., Monsignori Fossi, B.C., & Young, P.R. 1997, *A&AS*, 125, 149

- Dere, K.P. & Mason, H.E. 1993, *Sol. Phys.*, 123, 41
- Doschek, G.A., Feldman, U., Mariska, J.T., & Linsky, J.L. 1978, *ApJ*, 226, L35
- Dufton, P.L., Hibbert, A., Kingston, A.E., & Doschek, G.A. 1982, *ApJ*, 257, 338
- Feldman, U., Behring, W.E., Curdt, W., Schüle, U., Wilhelm, K., Lemaire, P. & Moran, T. 1997, *ApJS*, 113, 195
- Gilliland, R.L., & Hulbert, S.J. 1993, *GHRIS Instrument Sci. Rep.* 55
- Gray, D.F., *The observation and analysis of stellar photospheres*, (Cambridge: Cambridge University Press)
- Guirado, J.C. et al. 1997, *ApJ*, 490, 835
- Heap, S.R. et al. 1995, *PASP*, 107, 871
- Innis, J.L., Coates, D.W., Thompson, K., & Robinson, R.D. 1985, *Proc. Astron. Soc. Australia*, 6, 156
- Innis, J.L., Thompson, K., & Coates, D.W. 1986, *MNRAS*, 223, 183
- Jordan, C. 1975 *MNRAS*, 170, 429
- Kürster, M., Schmitt, J.H.M.M., Cutispoto, G., & Dennerl, K. 1997, *A&A*, 320, 831
- Lallement, R., & Bertin, P. 1992, *A&A*, 266, 479
- Lallement, R., Ferlet, R., Lagrange, A.M., Lemoine, M., & Vidal-Madjar, A. 1995, *A&A*, 304, 461
- Laming, J.M. & Feldman, U. 1993, *ApJ*, 403, 434
- Landini, M. & Monsignori Fossi, B.C. 1990, *A&AS*, 82, 229
- Linsky, J.L., & Wood, B.E. 1996, *ApJ*, 463, 254
- Mewe, R., Kaastra, J.S., White, S.M., & Pallavicini, R. 1996, *A&A*, 315, 170
- Pakull, M.W. 1981, *A&A*, 104, 33
- Piskunov, N., Wood, B.E., Linsky, J.L., Dempsey, R.C., & Ayres, T.R. 1997, *ApJ*, 474, 315
- Redfield, S., & Linsky, J.L. 2000, *ApJ*, 534, 825
- Robinson, R.D. & Cameron, A. 1986, *Proc. Astron. Soc. Australia*, 6, 308
- Robinson, R.D. et al. 1998, *PASP*, 110, 68
- Rucinski, S., Garrison, R.F., & Duffee, B. 1995a *IBVS* 4156
- Rucinski, S.M., Mewe, R., Kaastra, J.S., Vilhu, O., & White, S.M. 1995b *ApJ*, 449, 900
- Schmitt, J.H.M.M., Cutispoto, G., & Krautter, J. 1988, *ApJ*, 500, L25
- Vilhu, O., Ambruster, C., Neff, J.E., Linsky, J.L., Brandenberg, A., Ilyin, L.V., & Shakovskaya, N.I. 1989, *A&A*, 222, 179
- Vilhu, O., Gustafsson, B., & Walter, F.M. 1991, *A&A*, 241, 167

- Vilhu, O., Muhli, P., Huovelin, J., Hakala, P., Rucinski, S.M., & Cameron, A. 1998, *AJ*, 115, 610
- Wahlstrøm, C. & Carlsson, M 1994, *ApJ*, 433, 417
- Walter, F.M. et al. 1995, *BAAS*, 187, #103.05
- Walter, F.M. 1999, in *ASP Conf. Ser. 158, Solar and Stellar Activity: Similarities and Differences.* eds. C.J. Butler & J.G. Doyle (San Francisco: ASP), 87
- Walter, F.M. & Byrne, P.B. 1997, in *ASP Conf. Ser. 154, Cool Stars, Stellar Systems, and the Sun 10*, eds. R. Donahue & J. Bookbinder (San Francisco: ASP), CD-1458
- Wood, B.E., Linsky, J.L., & Ayres, T.R. 1997, *ApJ*, 478, 745
- Wood, B.E., Linsky, J.L., & Zank, G.P. 2000, *ApJ*, 537, 304
- Zirin, H. 1975, *ApJ*, 199, L63

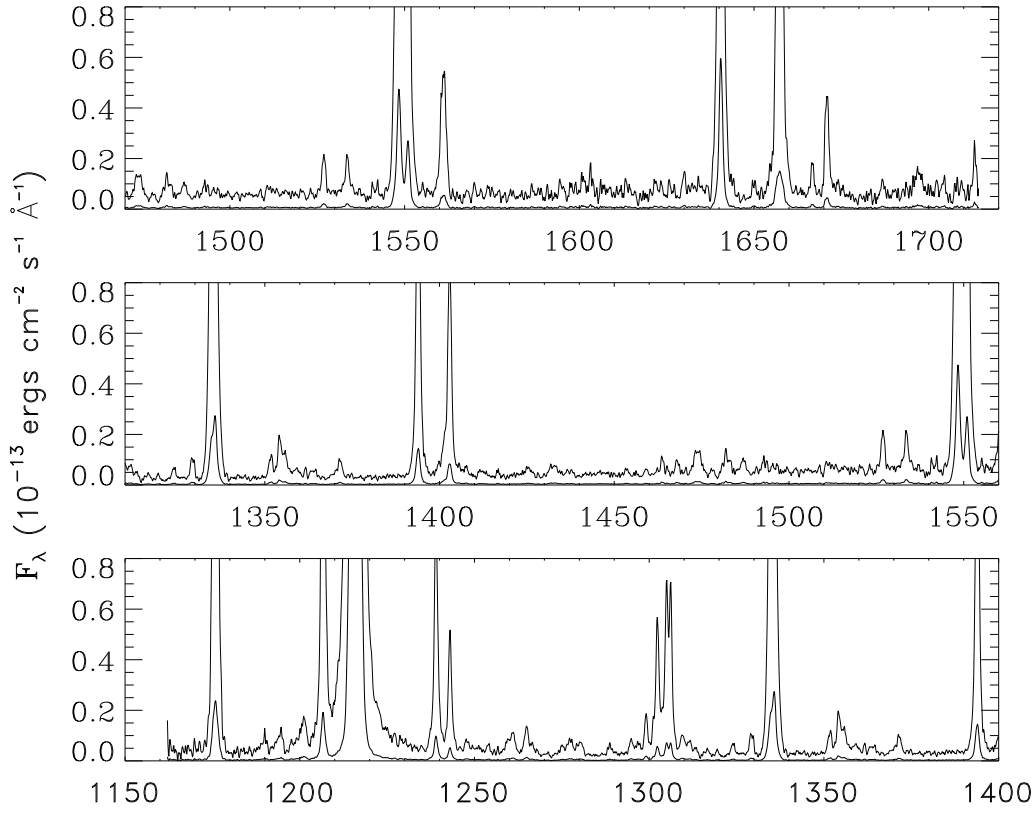


Fig. 1.— The summed low dispersion G440L spectrum of AB Dor between 1162 and 1714Å, smoothed with a Fourier filter. The data are binned into 0.14Å bins. The flux scale refers to the thin line; the thick line is scaled down by a factor of 10 to show the full dynamic range in the spectrum. Between 1428 and 1448Å, where the spectra overlap, the effective exposure time is 1688 s; elsewhere the exposure time is 844 s. Much of the Lyman α emission is geocoronal. Geocoronal O I λ 1304 is seen as a low broad pedestal under the narrow stellar lines.

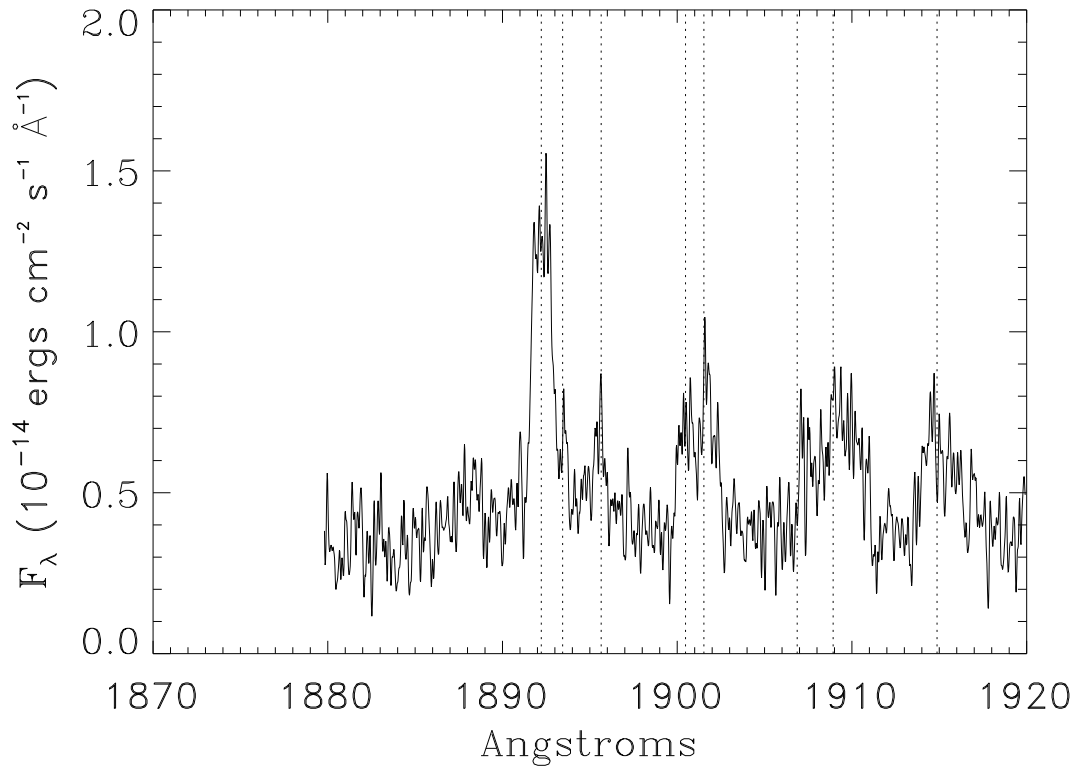


Fig. 2.— The mean G160M spectrum of the 1900Å region. The two observations have been averaged, and a Fourier filter has been applied. In addition to the Si III] λ 1892.03 and C III] λ 1908.734 lines, we see emission of S I $\lambda\lambda$ 1893.252, 1895.459, 1900.27, and 1914.68 and Si I λ 1901.338. There appears to be a narrow emission line at 1907.34Å. The C III] λ 1908.734 line is broader than the other lines, perhaps because it arises in low density regions well above the photosphere but co-rotating with the star. The dotted vertical lines mark the rest wavelengths of these lines at the stellar radial velocity.

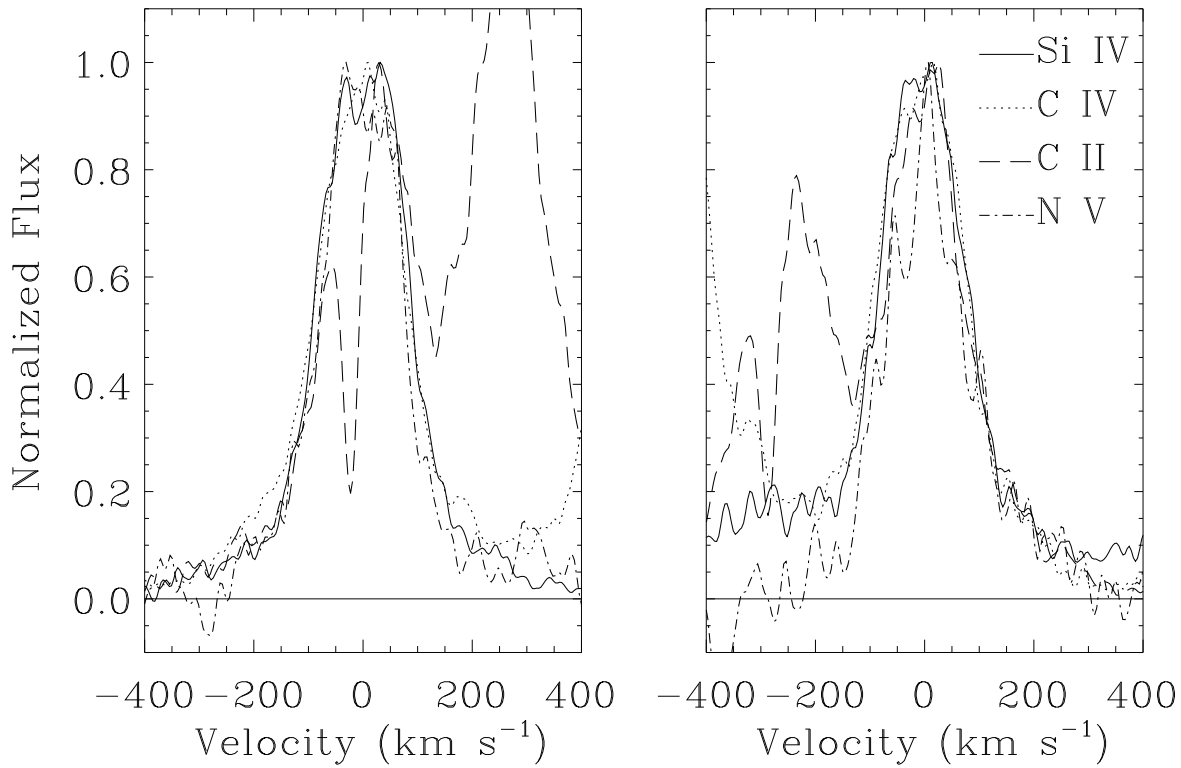


Fig. 3.— A comparison of the 4 transition region doublets in velocity space. The left panel shows the blueward line; the right panel shows the redward line. The normalized profiles are similar, with the following exceptions: the C II $\lambda 1334$ emission line includes a strong interstellar absorption feature; the blue wing of the Si IV $\lambda 1402$ line (right panel) is elevated due to O IV emission; and the N V $\lambda 1242$ line is noisy. The other component of the C II doublet is visible in each panel, and the wings of the C IV lines overlap.

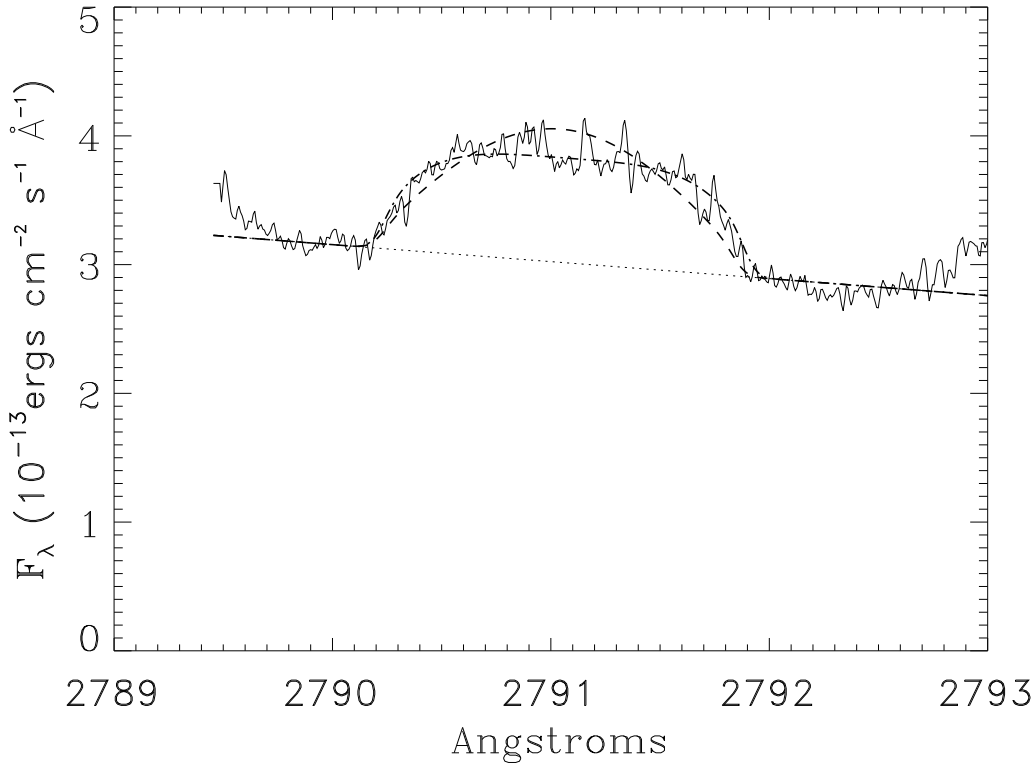


Fig. 4.— The subordinate $\lambda 2791$ line of Mg II. The data are the mean of 19 echelle observations. This line is almost certainly optically thin, and therefore represents the convolution of the surface distribution of Mg II with the rotational and thermal broadening. We show two fits to this line. The narrower profile (dashed) is the rotational profile for a limb-darkened surface ($\epsilon=0.6$); the broader profile (dash-dot), which better matches the data, is a limb-brightened atmosphere with a height of 2% of the stellar radius. Both profiles are rotationally broadened with $v \sin i=90 \text{ km s}^{-1}$, and have 5 km s^{-1} of thermal broadening. There is no evidence for non-thermal broadening at this level of the atmosphere. The dotted line is the extrapolated continuum.

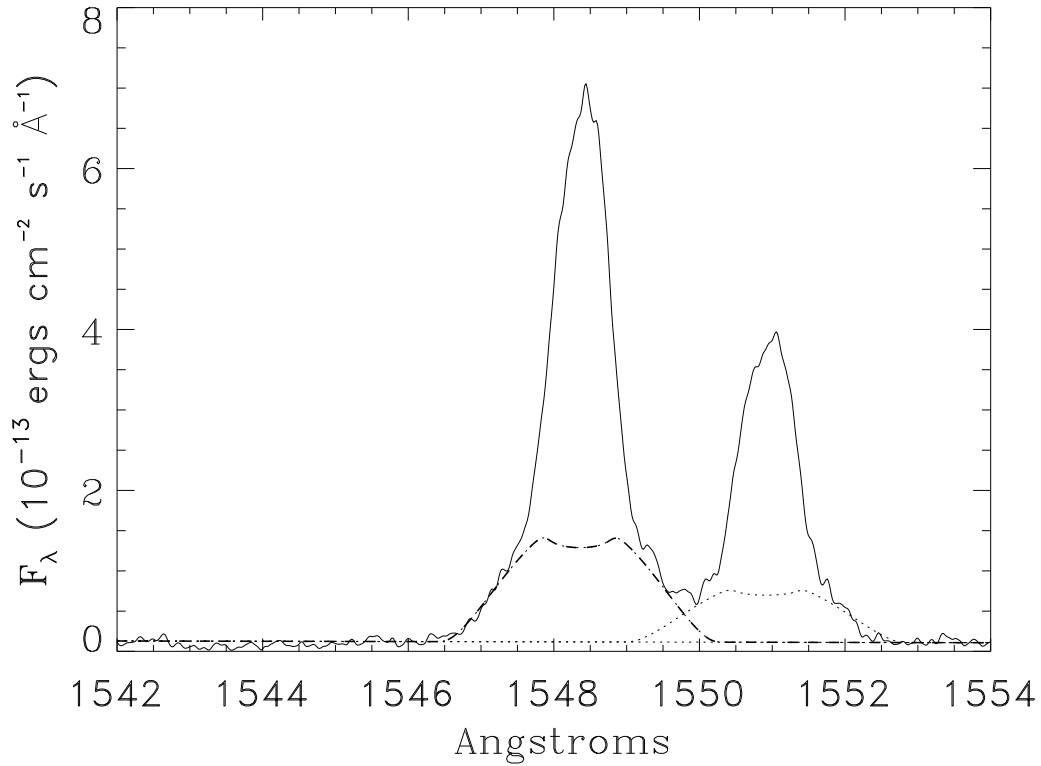


Fig. 5.— The mean quiescent C IV line profiles. The data have been smoothed with a Fourier filter. The dashed and dotted lines represent a model for emission from an optically-thin, constant density atmosphere extending out to 3 stellar radii. The model is centered on the rest wavelength of the line, and is scaled to the blue wing. The $\lambda 1551\text{\AA}$ line is not fit, but is assumed to be half the intensity of the $\lambda 1548\text{\AA}$ line.

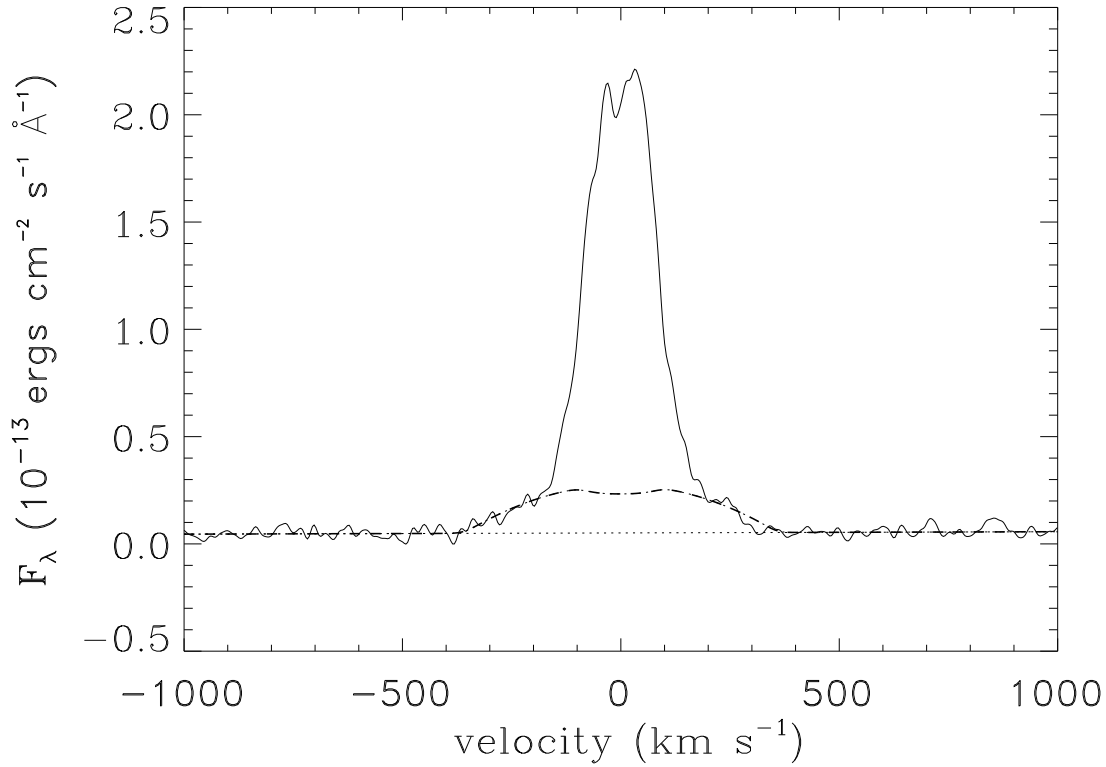


Fig. 6.— The mean quiescent Si IV $\lambda 1393$ line profile. The data have been smoothed with a Fourier filter. The dashed line represents a model for emission from an optically-thin, constant density atmosphere extending out to 3 stellar radii. The double-peaked line profile is not representative of any individual line, but is the consequence of summing 20 variable line profiles.

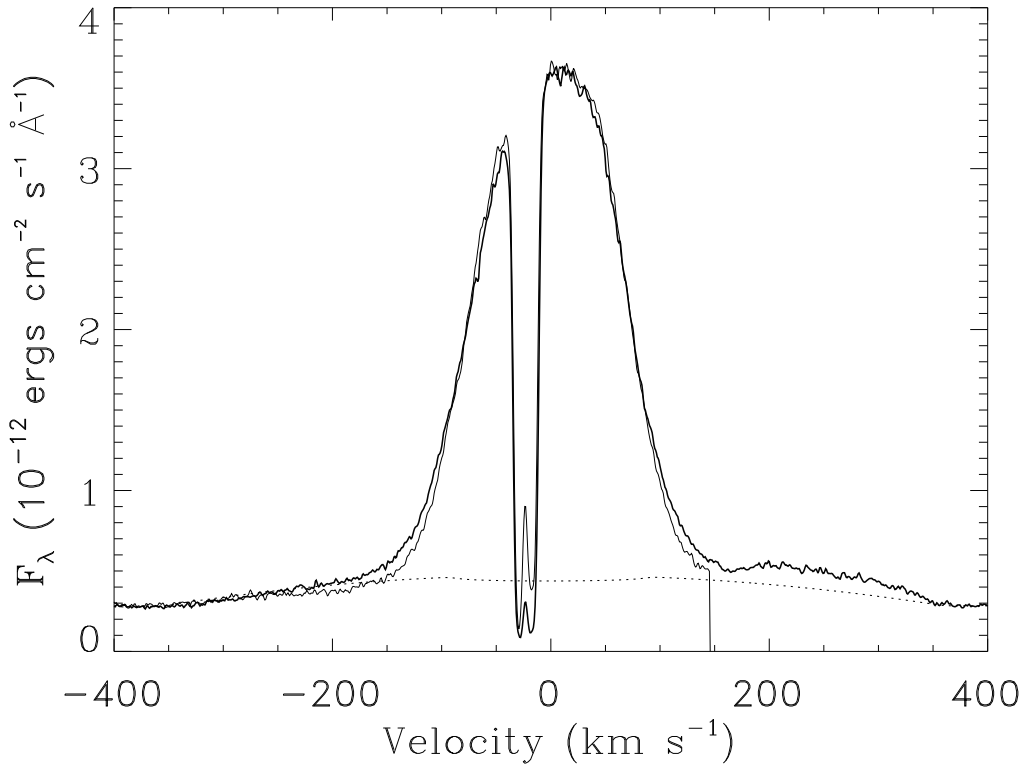


Fig. 7.— The mean Mg II line profiles. The thick line is the k line; the h line is overplotted as the thin line (the data are cut off at $+145 \text{ km s}^{-1}$ by the edge of the detector). The h line flux has been multiplied by a factor of 1.23 to match the line cores. The k line is brighter in the wings. The blue wing extends out to about -320 km s^{-1} . The hump on the red wing of the k line (between $+170$ and $+350 \text{ km s}^{-1}$) is the sum of the $\lambda 2797.922$ ($3p \ ^2P_{\frac{3}{2}} - 3d \ ^2D_{\frac{3}{2}}$) and $\lambda 2797.989$ ($3p \ ^2P_{\frac{3}{2}} - 3d \ ^2D_{\frac{3}{2}}$) subordinate lines of Mg II. The dotted line shows the expected emission line profile for an optically-thin uniform density extended atmosphere with a height of 3 stellar radii.

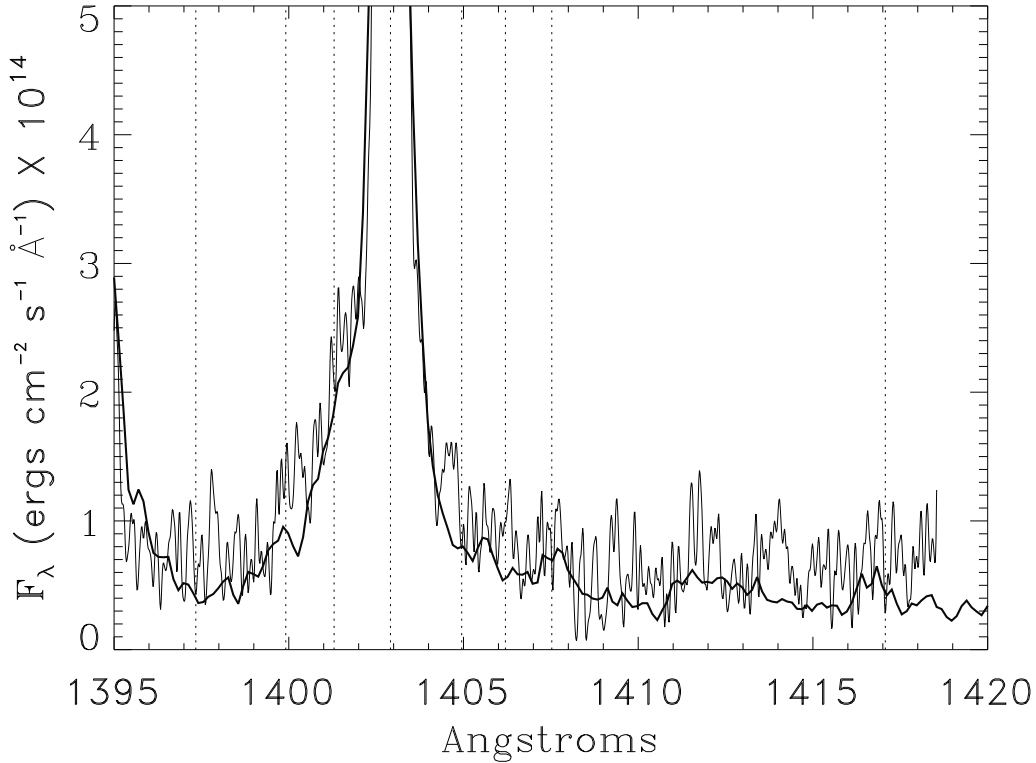


Fig. 8.— Spectra in the 1400Å region. The thin (noisier) line is the mean of 6 G160M observations (7368 seconds integration time); the thick line is the 844 second G140L spectrum. Both spectra have been smoothed with a Fourier filter. The strong emission line is Si IV λ 1402. Vertical dotted lines mark the expected locations of the O IV] and S IV] lines, at the +30 km s⁻¹ radial velocity of AB Dor. The clear asymmetry in the blue wing of the Si IV λ 1402 line is due to the O IV] λ 1399.8 and λ 1401.2 lines. There may also be weak detections of O IV] λ 1407.4 and S IV] λ 1416.9 in the low dispersion spectrum. The peak at λ 1404.6 in the G160M spectrum is at the wrong wavelength to be the λ 1404.8Å O IV]+S IV] blend. The other O IV] and S IV] lines are not detected in either spectrum.

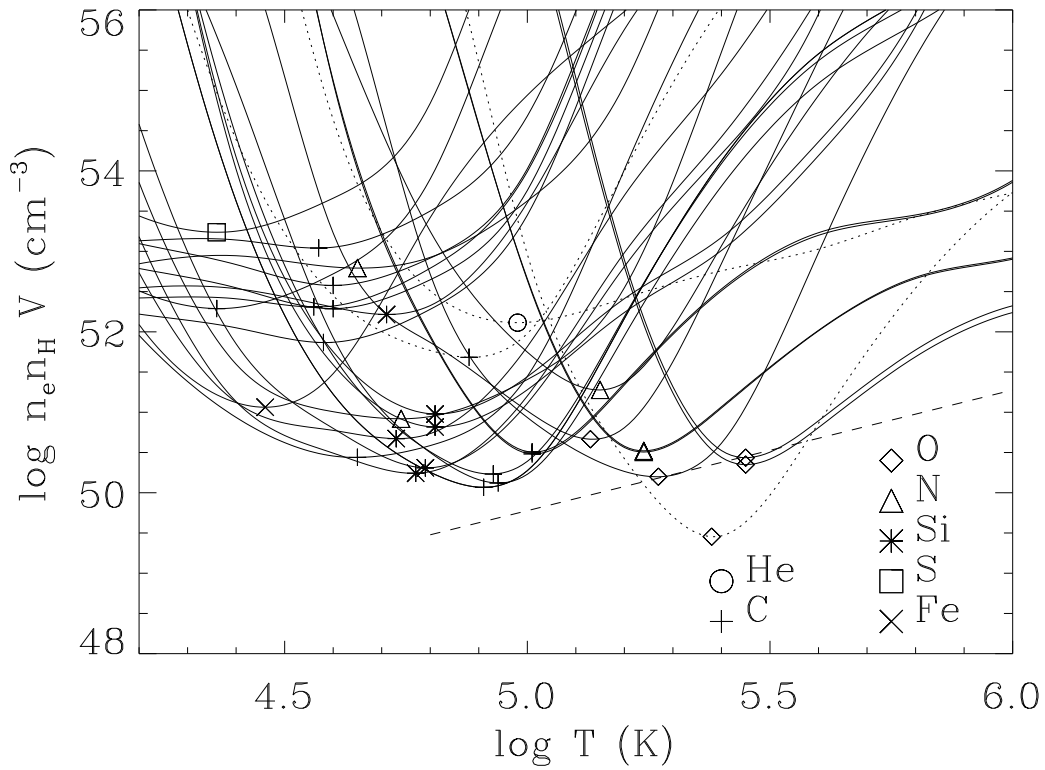


Fig. 9.— The emission measure diagram for AB Dor. Emissivities are from Landini & Monsignori Fossi (1990), for an assumed electron density of 10^{12} cm^{-3} . The emissivity curves have been interpolated with a cubic spline. FUV data from Schmitt, Cutispoto, & Krautter (1997) are included, as is the $T^{3/2}$ extrapolation of the coronal emission measure from Rucinski et al. (1995b). Symbols identifying the elements are plotted at the minimum emission measures for each curve. The O V $\lambda 1371$, He II $\lambda 1640$, and C III] $\lambda 1908$ emission measures, which are explicitly discussed in section 8 of the text, are shown as dotted lines.

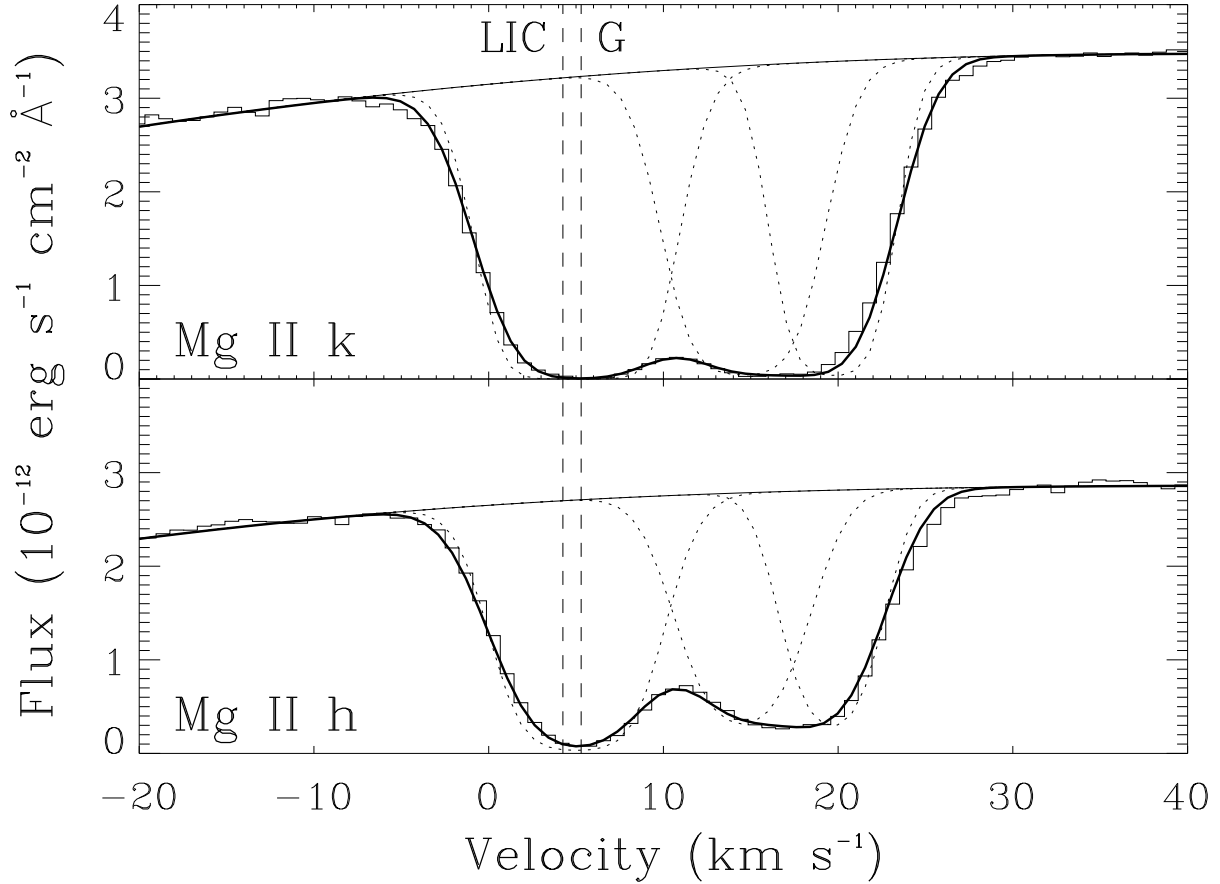


Fig. 10.— The ISM absorption features observed in the Mg II lines. The velocity scale is heliocentric. The data are shown in histogram form. Our best fit to the ISM lines is also shown (see Table 6 for the fit parameters). Fifth-degree polynomial fits to a mirrored line profile (*thin solid lines*) have been used to interpolate the intrinsic Mg II line profiles in the spectral regions where the ISM absorption is located. The absorption profiles of the three interstellar absorption components are shown as dotted lines, and the convolution of the profiles with the instrumental profile is shown as a thick solid line. Dashed vertical lines show the projected velocities of the LIC and G cloud flow vectors for the AB Dor line of sight.

Table 1. GHRs Observation Log

Root	Date (1994 Nov)	UT (start)	Grating	time (sec)	Phase ^a	Notes ^b
Z2I60107	14	23: 4:20	Ech-B	256	0.930	1
Z2I60109	14	23:12:23	G160M	1228	0.941	2
Z2I6010B	14	23:36: 4	Ech-B	256	0.973	1
Z2I6010D	14	23:43:51	G160M	1228	0.983	3
Z2I6010F	15	0: 8:38	Ech-B	256	1.017	1
Z2I6010H	G160M	1228	...	7
Z2I6010M	15	0:59: 2	Ech-B	256	1.085	1
Z2I6010O	15	1: 7: 5	G160M	1228	1.096	2
Z2I6010Q	15	1:30:46	Ech-B	256	1.128	1
Z2I6010S	15	1:38:33	G160M	1228	1.138	3
Z2I6010U	15	2: 5: 2	Ech-B	256	1.174	1
Z2I6010W	G160M	1228	...	7
Z2I60111	15	2:53:50	Ech-B	256	1.240	1
Z2I60113	15	3: 1:47	G160M	1228	1.250	2
Z2I60115	15	3:25:34	Ech-B	256	1.282	1
Z2I60117	15	3:33:21	G160M	1228	1.293	3
Z2I60119	15	3:57:16	Ech-B	256	1.325	1
Z2I6011B	15	4: 5:17	G160M	1228	1.336	4
Z2I6011G	15	4:48:38	Ech-B	256	1.394	1
Z2I6011I	15	4:56:35	G160M	1228	1.405	2
Z2I6011K	15	5:20: 8	Ech-B	256	1.437	1
Z2I6011M	15	5:28:17	G160M	1228	1.448	3
Z2I6011O	15	5:52: 4	Ech-B	256	1.480	1
Z2I6011Q	15	5:59:58	G160M	1228	1.491	5
Z2I6011V	15	6:43:20	Ech-B	256	1.549	1
Z2I6011X	15	6:51: 9	G160M	1228	1.560	2
Z2I6011Z	15	7:14:50	Ech-B	256	1.592	1
Z2I60121	15	7:23:11	G160M	1228	1.603	3
Z2I60123	15	7:46:52	Ech-B	256	1.635	1
Z2I60125	15	7:54:47	G160M	1228	1.646	6
Z2I6012A	15	8:38: 8	Ech-B	256	1.704	1
Z2I6012C	15	8:45:51	G160M	1228	1.714	2

Table 1—Continued

Root	Date (1994 Nov)	UT (start)	Grating	time (sec)	Phase ^a	Notes ^b
Z2I6012E	Ech-B	256	...	7
Z2I6012G	15	9:17:35	G160M	1228	1.757	3
Z2I6012I	15	9:41:31	Ech-B	256	1.790	1
Z2I6012K	15	9:49:21	G160M	1228	1.800	4
Z2I6012P	15	10:52:38	Ech-B	256	1.885	1
Z2I6012R	G160M	1228	...	7
Z2I6012T	15	11:22:52	Ech-B	256	1.926	1
Z2I6012V	15	12:45:21	G140L	844	2.038	8
Z2I6012W	15	13: 3:29	G140L	844	2.062	9

^aPhase at start of observation. Zero phase occurs at HJD 2444296.575. The rotation is 10440 plus the phase.

^b(1) Mg II h& K; (2) Si IV; (3) C IV; (4) Si III], C III]; (5) N V; (6) C II; (7) Observation failed; (8) low dispersion 1305Å; (9) low dispersion 1570Å

Table 2. Low Dispersion Line Atlas

λ	flux (10^{-14} erg cm $^{-2}$ s $^{-1}$)	Line Identification
1175.86	44.0 ± 0.4	C III λ 1175.711
1189.86	1.43 ± 0.28	S III λ 1190.17; Si II λ 1190.42
1194.41	1.68 ± 0.29	Si II λ 1193.29; S III $\lambda\lambda$ 1194.06,1194.46
1197.56	0.40 ± 0.18	Si II λ 1197.39
1201.13	2.77 ± 1.14	N I $\lambda\lambda$ 1200.22,1200.71; S III $\lambda\lambda$ 1200.97,1201.73
1206.68	24.9 ± 0.7	Si III λ 1206.51
1215.91	...	H I (\oplus)
1238.99	13.7 ± 0.28	N V λ 1238.82
1243.05	6.62 ± 0.25	N V λ 1242.80
1247.81	0.28 ± 0.16	C III λ 1247.38
1253.96	0.31 ± 0.10	Si II λ 1253.80
1259.57	0.96 ± 0.09	Si II λ 1259.53
1261.08	1.01 ± 0.08	C I λ 1261.3
1264.81	1.46 ± 0.09	Si II λ 1264.74
1266.50	0.74 ± 0.09	C I λ 1266.42
1275.04	0.52 ± 0.07	...
1277.33	1.19 ± 0.08	C I λ 1277.5
1280.14	0.98 ± 0.09	C I λ 1280.5
1288.77	0.64 ± 0.15	C I λ 1288.42
1294.87	0.70 ± 0.20	Si III λ 1294.54
1296.77	0.46 ± 0.28	Si III λ 1296.72
1299.09	1.31 ± 0.30	Si III λ 1298.89
1301.16	0.64 ± 0.07	Si III λ 1301.15
1302.33	5.27 ± 0.10	O I λ 1302.16
1304.97	5.27 ± 0.15	O I λ 1304.86
1306.12	7.06 ± 0.15	O I λ 1306.03
1309.59	0.90 ± 0.08	Si II λ 1309.28
1311.53	0.70 ± 0.09	C I λ 1311.36
1313.35	0.30 ± 0.08	...
1316.67	0.19 ± 0.06	S I λ 1316.54
1319.46	0.13 ± 0.06	N I λ 1319.00
1323.99	0.57 ± 0.16	S I λ 1323.52

Table 2—Continued

λ	flux (10^{-14} erg cm $^{-2}$ s $^{-1}$)	Line Identification
1329.28	1.17 ± 0.07	C I λ 1329.1
1334.74	22.8 ± 0.2	C II λ 1334.53
1335.83	35.2 ± 0.2	C II λ 1335.71
1351.76	1.34 ± 0.08	Cl I λ 1351.66
1354.16	1.90 ± 0.08	Fe XXI λ 1354.08
1355.71	1.83 ± 0.10	O I λ 1355.60
1358.91	0.92 ± 0.10	C I λ 1357.13; O I λ 1358.51
1361.63	0.27 ± 0.05	...
1363.27	0.29 ± 0.06	...
1364.44	0.37 ± 0.06	C I λ 1364.16
1370.27	0.14 ± 0.05	N III λ 1369.99
1371.53	1.06 ± 0.12	O V λ 1371.292
1393.89	21.3 ± 0.05	Si IV λ 1393.76
1399.72	0.65 ± 0.10	O IV] λ 1399.77
1401.34	1.24 ± 0.15	O IV] λ 1401.16
1402.90	12.0 ± 0.13	Si IV λ 1402.77
1407.68	0.24 ± 0.10	O IV] λ 1407.39
1412.59	0.34 ± 0.10	Fe II λ 1412.83
1416.71	0.25 ± 0.08	S IV] λ 1416.93
1424.04 ^a	0.14 ± 0.07	S IV] λ 1423.9
1425.41	0.73 ± 0.11	S I λ 1425.03
1432.43	1.07 ± 0.10	C I λ 1432.11
1459.14	0.11 ± 0.10	C I λ 1459.03
1463.72	1.02 ± 0.13	C I λ 1463.33; Fe X λ 1463.50
1468.00	0.79 ± 0.16	Fe IX λ 1467.06; C I λ 1467.4
1473.12	0.88 ± 0.12	S I λ 1472.97
1474.36	1.22 ± 0.13	S I λ 1474.00
1481.93	1.12 ± 0.13	S I λ 1481.67
1483.27	0.33 ± 0.08	S I λ 1483.23
1486.89	0.90 ± 0.13	N IV λ 1486.50; S I λ 1487.15
1492.98	0.85 ± 0.13	...
1526.89	2.14 ± 0.13	Si II λ 1526.71

Table 2—Continued

λ	flux (10^{-14} erg cm $^{-2}$ s $^{-1}$)	Line Identification
1533.66	2.71 ± 0.61	Si II λ 1533.43
1540.84	0.22 ± 0.10	Fe II λ 1541.03
1542.26	0.27 ± 0.09	C I λ 1542.18
1548.40	80.9 ± 0.7	C IV λ 1548.20
1550.94	42.7 ± 0.6	C IV λ 1550.77
1561.09	9.31 ± 0.24	C I λ 1561.00
1640.52	84.7 ± 0.89	He II λ 1640.48
1649.98	0.54 ± 0.19	Fe II $\lambda\lambda$ 1649.42,1649.57
1657.33	38.0 ± 0.71	C I $\lambda\lambda$ 1556.28,1556.97,1557.38,1558.01
1666.70	1.52 ± 0.19	O III] λ 1666.15
1670.86	5.87 ± 0.25	Fe II λ 1670.74
1686.79	0.42 ± 0.19	Fe II λ 1686.46
1697.03	2.40 ± 0.34	Fe II λ 1696.79
1713.18	1.64 ± 0.13	Fe II λ 1713.0

^aWavelength fixed; blended with S I λ 1425.03.

Table 3. Lines in $\lambda 1900\text{\AA}$ Spectral Region

λ^a	flux (10^{-14} erg cm $^{-2}$ s $^{-1}$)	FWHM \AA	Line Identification
1892.30 ± 0.01	1.51 ± 0.01	1.28 ± 0.05	Si III] $\lambda 1892.030$
1893.58 ± 0.02	0.09 ± 0.02	0.26 ± 0.07	S I $\lambda 1893.252$?
1895.39 ± 0.02	0.52 ± 0.03	0.63 ± 0.09	S I $\lambda 1895.459$
1900.48 ± 0.02	0.34 ± 0.01	0.81 ± 0.13	S I $\lambda 1900.270$
1901.74 ± 0.01	0.54 ± 0.01	0.94 ± 0.10	Si I $\lambda 1901.338$
1907.34 ± 0.04	0.25 ± 0.02	0.88 ± 0.16	
1909.38 ± 0.04	1.1 ± 0.1	2.09 ± 0.15	C III] $\lambda 1908.734^b$
1915.05 ± 0.04	0.75 ± 0.03	0.87 ± 0.24	S I $\lambda 1914.680$

^aObserved wavelength. The rest wavelengths are 0.19\AA smaller.

^bBroad line. See discussion in Section 7.4.

Table 4. Weak Lines in the G160M $\lambda 1400\text{\AA}$ Spectrum

λ^a	flux (10^{-14} erg cm $^{-2}$ s $^{-1}$)	Line Identification
1400.07 ± 0.04	0.5 ± 0.1	O IV] $\lambda 1399.77$
1401.58 ± 0.03	1.2 ± 0.3	O IV] $\lambda 1401.16$
1407.70 ± 0.02	0.26 ± 0.04	O IV] $\lambda 1407.39$

^aObserved wavelength. The rest wavelengths are 0.14\AA smaller.

Table 5. Density Diagnostics

Lines	ratio	$\log n_e$ (cm ⁻³)	$\log n_e$ (cm ⁻³) ^a
$\frac{\text{Si III } \lambda 1206}{\text{Si III } \lambda 1892}$	16.5 ± 0.5	12.2 ± 0.1	
$\frac{\text{Si III } \lambda 1301}{\text{Si III } \lambda 1892}$	0.42 ± 0.05	12.5 ± 0.1	
$\frac{\text{Si III } \lambda \lambda 1294-1301}{\text{Si III } \lambda 1892}$	2.0 ± 0.2	12.2 ± 0.1	
$\frac{\text{Si III } \lambda \lambda 1294-1301}{\text{Si III } \lambda 1206}$	0.12 ± 0.01	$12.2^{+0.4}_{-0.8}$	
$\frac{\text{C III } \lambda 1247}{\text{C III } \lambda 1908}$	0.25 ± 0.14	$11.1^{+0.4}_{-0.2}$	
$\frac{\text{C III } \lambda 1175}{\text{C III } \lambda 1247}$	157 ± 89	$9.1^{+1.1}_{-0.8}$	$11.8^{+2.8}_{-0.8}$
$\frac{\text{C III } \lambda 1175}{\text{C III } \lambda 1908}$	39 ± 1	10.8 ± 0.1	11.1 ± 0.1
$\frac{\text{Si IV } \lambda 1402}{\text{C III } \lambda 1908}$	10.6 ± 0.5	11.5 ± 0.1	
$\frac{\text{Si III } \lambda 1892}{\text{C III } \lambda 1908}$	1.3 ± 0.1	10.5 ± 0.1	

^aDensity computed after doubling the C III $\lambda 1175$ flux. See Section 7.2.

Table 6. Fit Parameters for the Mg II Interstellar Components

Component	v (km s ⁻¹)	b (km s ⁻¹)	$\log N_{\text{MgII}}$ $\log(\text{cm}^{-2})$
1	5.2 ± 0.1	3.8 ± 0.1	13.13 ± 0.06
2	14.5 ± 0.8	3.0 ± 0.8	12.8 ± 0.4
3	19.6 ± 0.7	2.8 ± 0.5	12.7 ± 0.2